IEEE Access
Multidisciplinary | Rapid Review | Open Access Journal

Received July 31, 2019, accepted August 26, 2019, date of publication August 29, 2019, date of current version September 20, 2019.

Digital Object Identifier 10.1109/ACCESS.2019.2938313

Investigation on the Thermal Performance of a 363 kV Vacuum Circuit Breaker Using a 3D Coupled Model

XIAO YU[1], FAN YANG[1], (Member, IEEE), GAO BING[1], HENG LIU[1], XING LI[1], SHAOGUI AI[2], AND XUXIANG WU[3]

[1]State Key Laboratory of Power Transmission Equipment and System Security and New Technology, School of Electrical Engineering, Chongqing University, Chongqing 400044, China
[2]Electric Power Research Institute, Ningxia Electric Power Company, State Grid Corporation of China, Yinchuan 750001, China
[3]Zhejiang Hangzhou Power Supply Company, State Grid Corporation of China, Hangzhou 310007, China

Corresponding author: Fan Yang (yangfancqu@gmail.com)

This work was supported by the Science and Technology Project of State Grid Corporation of China, through the Research on Key Technologies of Power Electronic Operation Control in Power System.

ABSTRACT Multi-break vacuum circuit breakers (VCBs) are the most potential approach for applying VCBs to high voltage power system. However, it has higher thermal stability requirements than normal single break VCBs due to its complex structure and high rated current. In this paper, a novel 363 kV/5000 A/63 kA SF_6 gas insulate (GI) VCB with series and parallel structure is proposed. To analyze its temperature rise, a 3D coupled electromagnetic-thermal–fluid model is established based on actual size and calculated by finite element method under rated condition, which enables prediction of the temperature distribution of the contacts of VCB and bus bar. In the numerical model, the vacuum chamber is modelled as solid material with temperature dependent effective thermal conductivity while skin effect, nonlinear property of conductor resistivity and turbulence model are taken into consideration. The simulation results show that the hot spot is the contacts of VCB with a temperature of 102.2 K, while the temperature of busbars reach at 92.3 K. In addition, the influences of contact resistance, short circuit current on the temperature rise are discussed. Finally, the simulation results are validated by temperature rise experiment on prototype. Using the proposed model, the temperature rise and hot spot area can be predicted in advance, which could finally facilitate the design and performance evaluation of the 363 kV GI-VCB.

INDEX TERMS Vacuum circuit breaker, temperature rise, coupled model, turbulence model, contact resistance.

I. INTRODUCTION

High voltage circuit breakers are key components of power system, which are designed to switch the rated current and interrupt the inrush fault current during normal operating conditions and short circuit conditions. Once the short circuit current is detected, circuit breakers' contacts will open immediately to interrupt the fault current and extinguish the arc. However, as the power system is developing towards larger scale, other electrical devices such as transformers will suffer from the excess current before the fault current is completely extinguished. Therefore, high voltage power system has much higher requirements for fault current interruption time. Recently, high voltage VCBs with permanent magnetic actuators which could interrupt the current in a shorter period than the SF_6 circuit breakers due to their high reliability and controllability are attracted substantial attention [1]–[4]. In HV VCBs, the heating problem is more severe than those filled with oil or air, because the contact conductors are enveloped in a well-sealed vacuum chamber where the heat produced at the contact dissipates through the top and bottom conductors [5]. In order to avoid the overheating inside the VCBs, designers should pay attention to its heat production and transfer mechanism [6].

In this paper, we proposed a novel 363 kV gas (SF_6) insulated VCB (GI-VCB) which incorporated 12 low voltage

The associate editor coordinating the review of this manuscript and approving it for publication was Jason Gu.

VCBs connected both in parallel and series. Heating process in the gas insulated VCBs is more complicated. The conductors sealed in a vacuum chamber are supposed to have the highest temperature, but their temperature is hard to measure and also influenced by the heat conduction and convection of SF_6. Moreover, the related international standards including IEC and ANSI limit that the temperature-rise of the various parts of the power equipment should not exceed its specified values, and the regulations are becoming stricter for new products especially for the compact metal encapsulated devices [5]. Excessive temperature elevation results in aging or even thermal destruction of the components [7]. Hence, it is of great importance to analyze the thermal behavior before expensive and time-consuming experiments.

Some studies have been carried out on the calculation of temperature rise and gas flow of the circuit breakers and switchgears. Bedkowski *et al.* [7]–[9] built the 2.5D and 3-D coupled model of low-voltage switchgear to investigate the heat transfer process and analyzed the cooling effects on the reduction of losses, and they discussed different coupling way in the calculation of these models. Skin effect of conductors was suggested to take into consideration. Wang *et al.* [10] presented a coupling simulation of electromagnetic-thermal-flow field of a 12 kV medium voltage switchgear and the effect of gas flow field distribution was discussed in detail. Delgado *et al.* [11] investigated the thermal behavior of an industrial low voltage non-segregated three-phase busduct by means of the comparison of a 3D numerical model with experimental results. Compared to the switchgears, gas insulated VCBs are well-sealed in metal tank and the gas flow circulatory inner the tank. Dhotre *et al.* [12], [13] used the computational fluid dynamics (CFD) simulation to optimize the structure and reduce the new product development cycle time of the SF_6 gas circuit breaker, and used a thermal model based on ANSYS-CFX to predict the temperature rise of a high voltage SF_6 gas circuit breaker during a heat-run test. Pawar *et al.* [14] presented the coupling of CFD with computational electromagnetics (CE) to analyze the temperature distribution and gas flow of the high voltage SF_6 circuit breaker at different operation current. For VCBs, Lee *et al.* [15] calculated the temperature rise of 72.5 kV VCBs and found that error was less than 10% with both two methods by using the CFD model and thermal network analysis (TNA) method. Though the TNA model has high calculation efficiency, it's difficult to implement in complex structure apparatuses. Therefore, numerical simulations can provide accurate predictions of temperature rise for power apparatuses under well-constructed models.

However, up to now, few researches about GI-VCB and its thermal analysis installed in high pressure gas tank have been reported. For a novel high-voltage GI-VCB, modeling and simulation is very important for its design and optimization. The structure of this circuit breaker is so complicated that it is difficult to calculate the temperature directly. Hence, a thorough thermal analysis should be incorporated into the design process of new type circuit breaker before type test. This paper aims at specifying the hotspot temperature of the proposed novel 363 kV GI-VCB during a temperature rise test considering skin effect, nonlinear property of conductor resistivity and coupling of the electromagnetic field, temperature field and fluid field. Its thermal behavior in the steady state is elaborated using the 3D coupled electromagnetic-thermal-fluid model and the simulation results are compared with the experimental results. Furthermore, the effect of contact resistance and short circuit current were discussed.

The remainder of this paper is organized as follows, in Section 2, we overview the design and structure of the novel 363 kV GI-VCB. In Section 3, we present the coupled model to simulate the temperature rise and gas flow. In Section 4, calculation results are presented and are validated with experimental data. Section 5 will discuss main influence factors. Finally, conclusions are drawn in Section 6.

II. STRUCTURE OF THE 363 KV GI-VCB

The 363 kV GI-VCB is composed of 40.5 kV VCBs. Fig.1 shows the schematic of the designed prototype. There are two branches: six VCBs are connected in series and six VCBs are in parallel. All the VCBs are enclosed with an aluminum alloy tank filled with 0.4MPa SF_6, as shown in Fig. 1 (a).

Its rated current is 5000 A and rated short-circuit breaking current is 63 kA. The internal detailed structure and cross section of the 40.5 kV VCB are shown in Fig. 1(b). The VCBs are sealed in a vacuum chamber made of ceramic, and are connected to the bottom actuator through insulating tension pole. Besides, VCBs are supported by cylindrical epoxy braces to make sure adequate insulation allowance. The actuator is driven by electromagnetic repulsion mechanism which can reduce the opening time to 5ms. The uneven degree of the current is small than 1.1 even during in the opening process according to our test.

Large and complex 3D geometries are often computationally expensive. The structure of the whole 363 kV GI-VCB is very complicated and the size is 2 meters in height and 9 meters in length, making it impossible to perform calculations in reasonable time. Hence, it is very difficult to simulate the heating process of the whole machine. As a preliminary design study and fundamental research, considering the symmetry of the whole structure, it is reasonable to analyze the thermal performance of single unit of the 363 kV GI-VCB because we mainly focus on the temperature of the vacuum interrupter conductors and the bus bars. To simplify the simulation model, screws, caps, bolts, rod pieces, shields of the VCB and the actuator are ignored, since they have little influence on the electromagnetic field and heat losses [1], [10], [21]. And the supporting construction, which is made of epoxy resin (insulation material), also has little influence on thermal performance of the device are also removed. The whole operating mechanism is replaced by a relatively simple metal block shell, because the electromagnetic field is shielded by this shell so there are almost no losses inner the shell. Small geometry features (fillets, chamfers, etc.) are also omitted to reduce the meshes. An example of simplification is

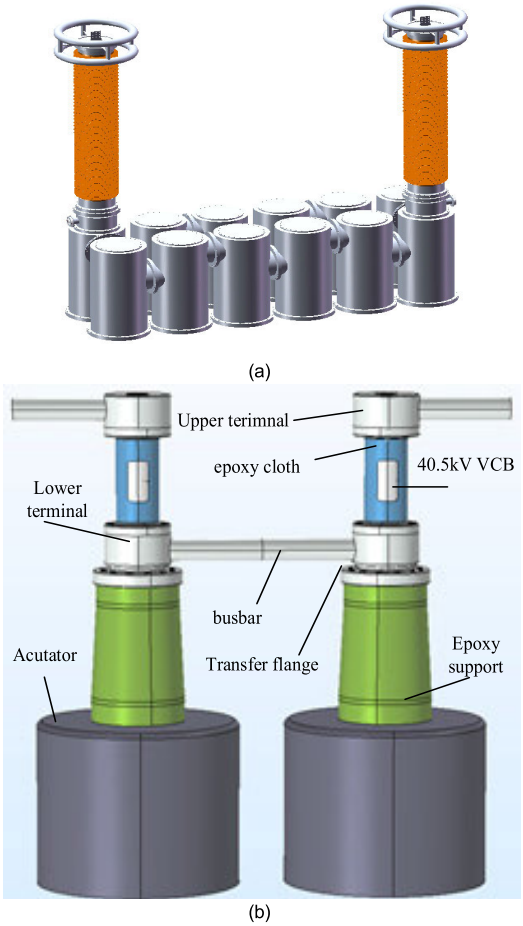

FIGURE 1. Structure of the 363 kV GI-VCB. (a) Overall structure. (b) Inner details.

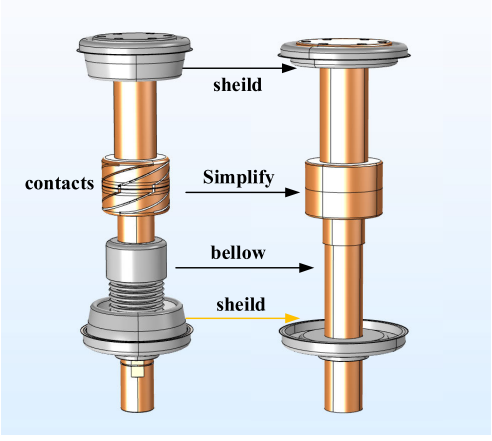

FIGURE 2. Simplification of 40.5 kV VCB.

given in Fig. 2, where the contacts are simplified to a cylinder where bellow and end shield are removed. Because the power losses are generated in the conducting busbars and aluminum alloy tank, a realistic presentation of the busbar's geometry is required. Table 1 and Table 2 show some parameters of the 363 kV GI-VCB.

TABLE 1. Parameters of the single unit of 363 kV GI-VCB.

Parameter name	Value
Outer diameter of the tank	410 mm
Height of the tank	2047 mm
Outer diameter of the busbar	80 mm
Inner diameter of the busbar	64 mm
Diameter of the Terminal	156 mm
Diameter of Transfer flange	245 mm

TABLE 2. Parameters of the 40.5 kV VCB.

Parameter name	Value
Length of moving contact	190 mm
Length of static contact	105 mm
Diameter of contact	40 mm
Thickness of contact s	30 mm
Round diameter of contacts	8 mm
External diameter of ceramic envelope	480 mm
Thickness of ceramic envelope	8.5 mm
Internal diameter of ceramic envelope	400 mm
Height of ceramic envelope	378mm

III. COUPLED MODELS AND CALCULATION

A. HEAT TRANSFER ANALYSIS

When the GI-VCB operates at rated condition, the 50 Hz alternating current passes through its conductors, some proportion of the electricity in the conducting part are converted into heat, then the heat results in the SF_6 gas flow and temperature rise. The generated heat transfers through conduction, convection and radiation. Electrical conductivity of conductive materials and gas parameters depend on the temperature. Thus, the electromagnetic analysis, thermal analysis and gas flow analysis are coupled to each other. Fig. 3 illustrates the heat transfer path of the single GI-VCB.

B. ELECTROMAGNETIC MODEL

Heat sources are the ohmic and eddy current losses of the inner conductors and external tank. In order to accurately predict the thermal performance of this circuit breaker, electromagnetic simulation is performed using the magnetic vector potential $\boldsymbol{A}$, according to Maxwell equations [16], the quasi-static magnetic field problem can be described as follows:

$$\nabla \times \frac{1}{\mu_B}(\nabla \times \boldsymbol{A}) = \boldsymbol{J}_s - \sigma(T)\frac{\partial \boldsymbol{A}}{\partial t} \tag{1}$$

where μ_B is permeability, $\boldsymbol{A}$ is magnetic vector potential, $\boldsymbol{J}_S$ is source current density, $\sigma(T)$ is the conductivity of the materials for the desired temperature range (20–120°C). Relationship between conductivity of conductors and the

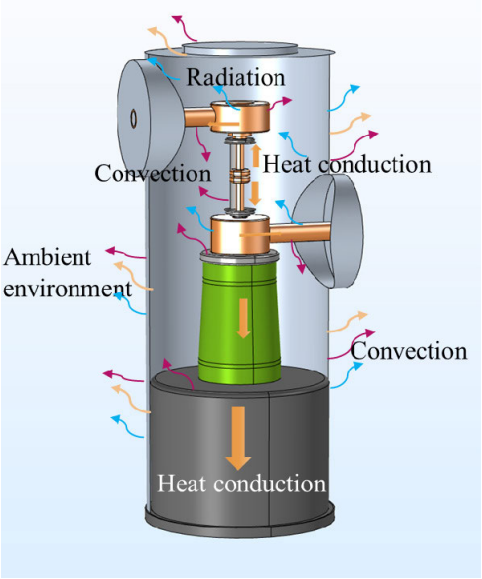

FIGURE 3. Heat transfer path of the 363 kV GI-VCB.

temperature is as follows:

$$\sigma(T) = \frac{\sigma_{20}}{1 + \alpha(T - 20)} \tag{2}$$

where σ_{20} is the conductivity at 20°C; α is the temperature coefficient; T is the conductor temperature.

As a result, the power loss Q_v is calculated by below equation:

$$Q_v = \int_V \frac{1}{\sigma(T)} \left| \boldsymbol{J}_s - \sigma(T) \frac{\partial \boldsymbol{A}}{\partial t} \right|^2 dV \tag{3}$$

C. THERMAL AND FLUID MODEL

A significant portion of heat generated in the inner conducting components is transferred to gas and tank, and then the ambient air. Hence, convection of SF_6 become crucial. Based on the actual size, gas properties and maximum flow rate of the model, the k-ε turbulence model is used to describe the complicated fluid flow and heat transfer process. This model has been successfully used for calculating the gas flow in longitudinal horizontal and vertical ducts [17], [18] and for simulation of buoyancy driven flows in ducts [19] and enclosures [7]–[9], [21]. Turbulence effects are modelled using the standard two-equation k-ε model with realizability constraints. The k-ε turbulence are the Reynolds-averaged Navier-Stokes equations for conservation of momentum, mass and the continuity equation for conservation of mass. The flow near walls is modelled using wall functions. The heat transfer module and turbulence module are coupled through non-isothermal interface in COMSOL Multi-physics software. The governing equations [22], [23] are shown below:

Conservation of momentum:

$$\rho \frac{\partial \boldsymbol{u}}{\partial t} + \rho(\boldsymbol{u} \cdot \nabla)\boldsymbol{u} = \nabla \cdot [-p\boldsymbol{I} + \mathbf{K})] + \boldsymbol{F} \tag{4}$$

$$\mathbf{K} = (\mu + \mu_T)\left(\nabla \boldsymbol{u} + (\nabla \boldsymbol{u})^T\right) - \frac{2}{3}(\mu + \mu_T)(\nabla \cdot \boldsymbol{u})\boldsymbol{I} - \frac{2}{3}\rho k \boldsymbol{I} \tag{5}$$

where ρ is the material density; $\boldsymbol{u}$ is the velocity vector, p is the gas pressure; $\boldsymbol{I}$ is the identity matrix; $\mathbf{K}$ is the viscous stress tensor; $\boldsymbol{F}$ is the body force per unit mass; μ is the dynamic viscosity,; μ_T is the eddy viscosity also called turbulent viscosity; k is the turbulent kinetic energy. C_μ is a model constant;

The turbulent viscosity is modeled as,

$$\mu_T = \rho C_\mu \frac{k^2}{\varepsilon} \tag{6}$$

where C_μ is a model constant; ε is the turbulent dissipation rate.

The transport equation for k is

$$\rho \frac{\partial \boldsymbol{u}}{\partial t} + \rho(\boldsymbol{u} \cdot \nabla)k = \nabla \cdot \left[\left(\mu + \frac{\mu_T}{\sigma_k}\right)\nabla k\right] + \boldsymbol{P}_k - \rho\varepsilon \tag{7}$$

where the production term $\boldsymbol{P}_k$ is

$$\boldsymbol{P}_k = \mu_T \left[\nabla \boldsymbol{u} : \left(\nabla \boldsymbol{u} + (\nabla \boldsymbol{u})^T\right) - \frac{2}{3}(\nabla \cdot \boldsymbol{u})^2\right] - \frac{2}{3}\rho k \nabla \cdot \boldsymbol{u} \tag{8}$$

The transport equation for ε is

$$\rho \frac{\partial \boldsymbol{u}}{\partial t} + \rho(\boldsymbol{u} \cdot \nabla)\varepsilon = \nabla \cdot \left[\left(\mu + \frac{\mu_T}{\sigma_\varepsilon}\right)\nabla \varepsilon\right] + C_{\varepsilon 1}\frac{\varepsilon}{k}\boldsymbol{P}_k - C_{\varepsilon 2}\rho\frac{\varepsilon^2}{k} \tag{9}$$

where σ_ε, $C_{\varepsilon 1}$ and $C_{\varepsilon 2}$ are the model constant.

Conservation of mass:

$$\frac{\partial \rho}{\partial t} + \nabla \cdot (\rho \boldsymbol{u}) = 0 \tag{10}$$

Conservation energy

$$\rho C_p \frac{\partial T}{\partial t} + \rho C_p \boldsymbol{u} \cdot \nabla T + \nabla \cdot \boldsymbol{q} = Q_v \tag{11}$$

Heat transfer by conduction

$$\boldsymbol{q} = -\lambda \nabla T \tag{12}$$

where T is temperature, $\boldsymbol{q}$ is the conductive heat flux; λ is the heat conductivity.

Since there is surface to surface radiation in the vacuum chamber, it can't be taken as thermal insulation medium inside the chamber. In the simulation, vacuum chamber inside poles is modelled as solid material with the temperature dependent effective thermal conductivity calculated from the following equation [21]:

$$k_{eff}(T) = \frac{2\sigma_0 T^3 \ln\left(\frac{d_{out}}{d_{in}}\right)}{\frac{1}{\varepsilon_{in} d_{in}} + \frac{1-\varepsilon_{out}}{\varepsilon_{out} d_{out}}} \tag{13}$$

In the above equation, σ_0 is the Stefan-Boltzmann constant; d_{out} and d_{in} stands for the diameter of the vacuum chamber and the conductor rod respectively. And ε_{out} and ε_{in} describes the corresponding surfaces emissivity.

D. BOUNDARIES AND MATERIAL PROPERTIES

According to the IEC standard [2], [24] and China's national standard [25], [26], the temperature of components and materials of the gas insulated switchgear are not allowed to exceed the limitations when the ambient temperature is less than 40°C. Hence, considering the severe condition, the ambient temperature is set to be 40°C, and the applied current is 2500 A sinusoidal current. Heat finally transfers to the surrounding air through convection and radiation. The computational domain is limited to the tank and its inner part. Convection between the exterior surface of the tank and ambient air is modelled in a simplified way to save computational time by using the convection boundary conditions at the tank surface and ambient temperature of 40°C respectively. This boundary is described as follows:

$$-\lambda\frac{\partial T}{\partial \boldsymbol{n}} = h\,(T - T_{amb}) \tag{14}$$

where h is the heat transfer coefficient, $\boldsymbol{n}$ is the normal direction of the tank surface. Heat transfer coefficient values used in convection boundaries are estimated based on the theoretical equations given for vertical and horizontal walls using following equations [16].

$$P_r = \frac{c_p\mu}{\lambda} \tag{15}$$

$$Gr = \frac{g\alpha_v\Delta T l^3}{v^2} \tag{16}$$

$$Nu = C\,(G_r \cdot \mathrm{Pr})^n \tag{17}$$

$$h = \frac{\lambda}{l}Nu \tag{18}$$

where P_r is Prandtl number, Nu is Nusselt number, Gr is Grashof number, they are characteristic numbers of fluid proposed by similarity principle. C and n are the empirical coeffects depend on the value of Gr. In this model, C and n are 0.11 and 0.333 respectively. c_p is the specific heat capacity; μ is the dynamic viscosity; l is the characteristic length; g is the acceleration of gravity; α_v is fluid volume expansion coefficient; ΔT is the temperature difference between wall and environment.

The radiation problem can be divided into internal and external radiation. The internal radiation includes the interaction of surfaces inside the tank, whereas the external radiation is defined as the interaction of the outside tank surface with surroundings. According to the Stefan-Boltzmann law, the heat radiation on the conductor and tank surface can be described as follows:

$$-\lambda\frac{\partial T}{\partial \boldsymbol{n}} = \sigma_0\varepsilon\left(T_{con}^4 - T_{\tan i}^4\right) \tag{19}$$

$$-\lambda\frac{\partial T}{\partial \boldsymbol{n}} = \sigma_0\varepsilon\left(T_{\tan o}^4 - T_{amb}^4\right) \tag{20}$$

where σ_0 is the Stefan-Boltzmann constant; the ε is the surface emissivity which is assumed to be 0.7; T_{con} is the surface temperature of conductor, T_{tani} and T_{tano} is the interior and exterior surface of the tank.

To obtain the accurate temperature value, taking the influence of temperature on the SF_6 properties into consideration, here it is fitted by functions in fluid-thermal analysis [16]. The density, viscosity, heat conductivity is derived by equations (21)-(23).

$$\rho_{SF_6} = -2.134\times10^{-7}T^3 + 0.0003771T^2 - 0.2415T + 65.51 \tag{21}$$

$$v_{SF_6} = 1.18\times10^{-10}T^2 - 5.69\times10^{-8}T \tag{22}$$

$$k_{SF_6} = 1.9\times10^{-7}T^2 - 9.05\times10^{-5}T + 0.02065 \tag{23}$$

where the $\rho_{SF_6}, v_{SF_6}, k_{SF_6}$ is the density, viscosity and heat conductivity of SF_6, T is the local temperature.

Other materials parameters used in the simulation are shown in table 3.

TABLE 3. Material parameters of 363 kV GI-VCB simulation model.

Materials	Resistivity [Ω·m]	Density [Kg/m^3]	Thermal conductivity [W/m·K]	Specific heat capacity [J/(kg·K)]
Copper	1.68E-8	8960	387.6	385
Aluminum	2.77E-8	2700	160	900
Steel	6.9E-7	7800	44.5	475
Epoxy resin	2E3	2060	0.71	1000
Ceramics	2E3	3000	29.3	750

E. MESH AND CALCULATION

The 3D global calculation model is established based on the actual size of single unit prototype. The substantial difference in the model scales (i.e., busbars, contacts, gas domain) require additional attention during the discretization. We refine the boundary layers and conductors to precisely for both the skin effect and flow of gas. Additional requirement is related to proper representation of rounded surfaces to assure correct evaluation of losses.

The momentum equation is a nonlinear convection-diffusion equation which can easily become unstable if discretized using the Galerkin finite element method. The streamline diffusion and nonlinear solver are applied to solve the problem [22], [23]. Boundary layer are added to the meshes for considering the skin effect and fluid flow. The number of boundary layer is 8 and the boundary layer stretching factor is 1.2. Then, the free tetrahedral meshes and corner refinement are applied. The size for free tetrahedral is custom defined and the maximum element is 3mm. Finally, the minimum quality of each element is above 0.674 and consistent with the requirements of the direct and full coupled solver configuration. Fig.4 shows the boundary layer meshes for the simulation model. The models are coupled to each other and solved transiently and an iterative process between electromagnetic and thermal-fluid analysis is used. The simulation is implemented in the COMSOL Multiphysics and the calculation flow chart is shown in Fig.5. Meshes used for thermal simulation consists of around 3.4 million tetrahedron elements. The numerical calculation is carried out by server

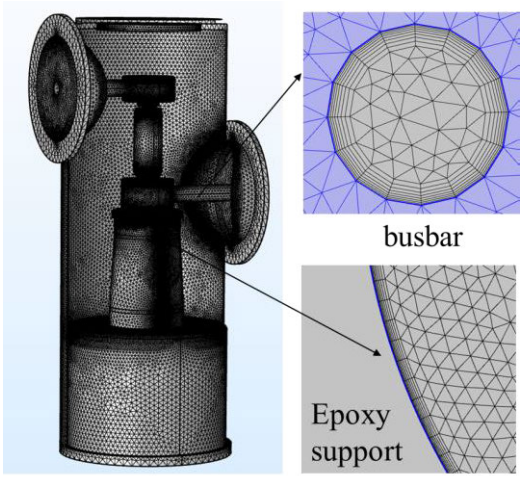

FIGURE 4. Mesh of the simulation model.

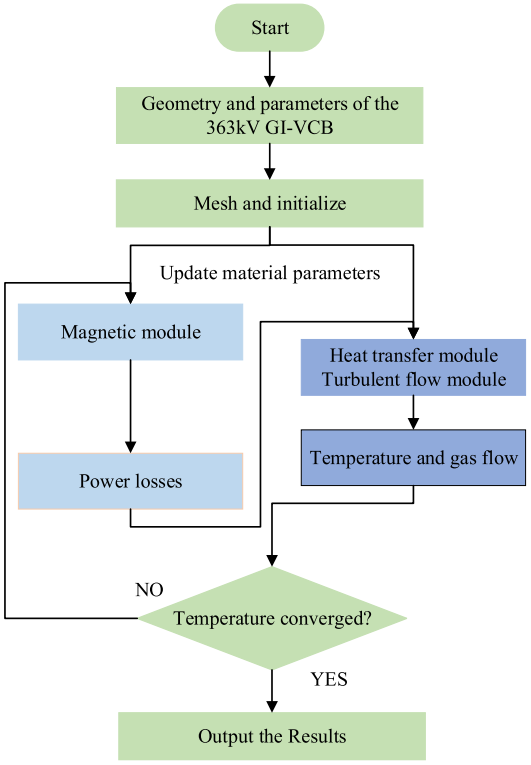

FIGURE 5. Simulation flow chart of the coupled model.

Intel Xeon with the RAM of 256 GB and cores of 32, and the calculation time is 41 h 23 min.

IV. RESULTS AND DISCUSSION

A. ELECTROMAGNETIC RESULTS

According to the calculation, electromagnetic field profile gives insight into the current density distribution in each conduction path. Distributions of the current density and magnetic field are shown in Fig.6. Maximum current density and power loss density appear on the surface of the conductors which emphasized the importance of skin effect. The

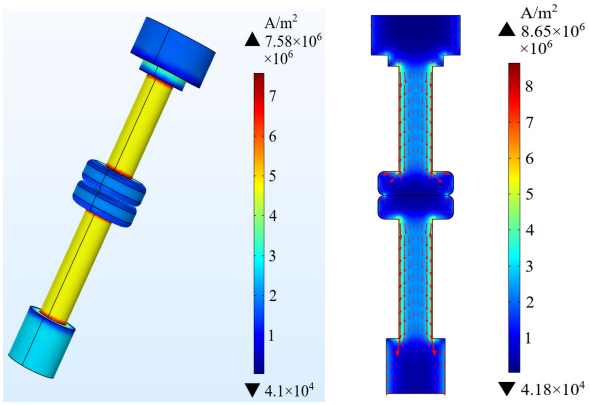

FIGURE 6. Current density of contacts of VCB and tank.

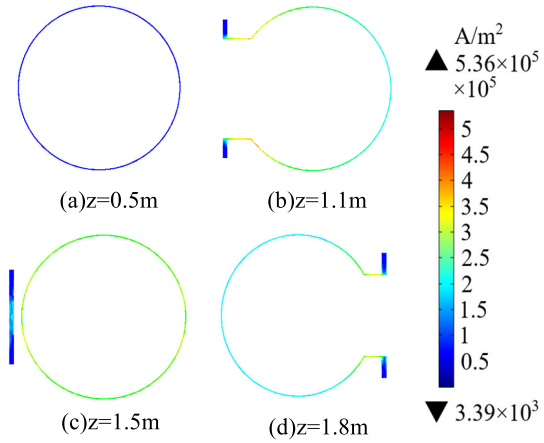

FIGURE 7. Cross sections of eddy current in the tank at different height.

current density of contacts is much small than other parts of conductor due to larger diameter of contacts and contacting rods. The maximum current density of contacts and static rod are 7.58E6 A/m^2 and 4.3E6 A/m^2. Current density in the upper terminal and bottom terminal are much smaller than the busbars and contacts because of bigger radius of 156mm. The maximum current in the bus bar is 3.15 E6 A/m^2. Nevertheless, the current density in the upper terminal and bottom terminal are 1.47E6 A/m^2 and 1.42E6 A/m^2, respectively, which are much smaller than busbars due to big radius.

The induced eddy current in the tank concentrated on the upper half part where current source is located. Eddy current distribution in the tank is shown in Fig. 7. The 4 cross sections are from bottom to up of the tank respectively. The eddy current density in the tank distributes unevenly due to the different distance to the inner conductors, and the maximum current density is 5.36E5 A/m^2 in the four cross sections. The eddy current near the connection part of tank is bigger than other parts because of the current flowing though the busbar. Power losses of contacts and busbars are 46.29 W and 48.96 W respectively. The total power losses generated by 2500A AC is 112.6 W, while the power loss of tank is only 2.21 W accounting for 1.96% of the total power losses.

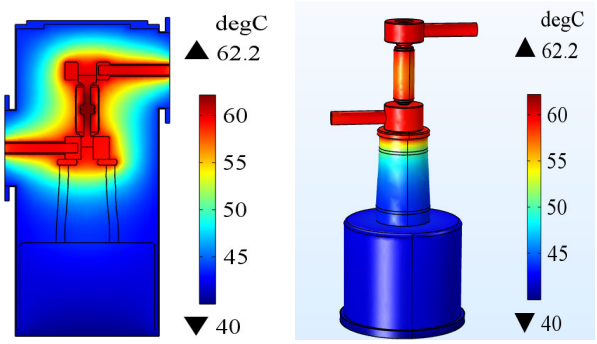

FIGURE 8. Temperature distribution of the 363 kV GI-VCB.

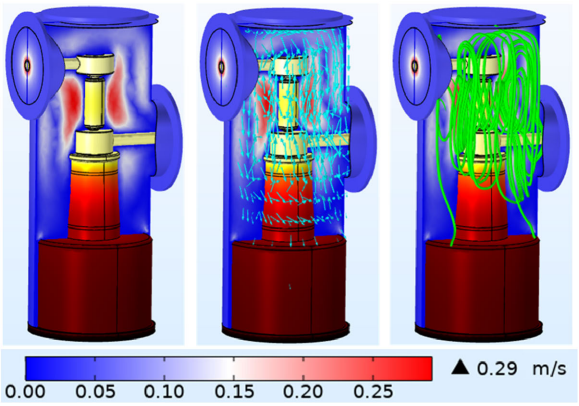

FIGURE 9. Fluid flow of the 363 kV GI-VCB with arrows and streamlines.

B. THERMAL AND FLUID RESULTS

The simulated temperature distribution is shown in Fig. 8. As expected, hotspot occurred in the middle part of the 363 kV GI-VCB, reaching at 102.2°C. The hotspot is the contacts of 40.5kV VCB, with the temperature rise of 62.2°C, while the temperature rise of busbar is 52.3°C which is under the limit of 65°C set by the IEC standard (IEC62271-100) [2], [24]–[26]. Temperature rise of the upper terminal and bottom terminal are 53.2°C and 50.4°C respectively. The temperature of busbars is third highest due to its hollow cylinder structure. Heat dissipation rate of conductors was reduced due to it is sealed in the vacuum chamber and heat losses are intensified as a result of skin effect and the nonlinear property of the copper conductivity. However, the upper terminal and bottom terminal as well as the busbars have large volume and section area that can be act as the role of heat sink through heat conduction for the conductors in the vacuum chamber. The heat of contacts mainly transfers to the connection terminals by conduction because they are isolated in the vacuum chamber which is modelled as an equivalent low heat conductivity material, while busbar's heat dissipates dominating through the convection of SF_6. The maximum temperature rise of outer tank is just 6.3 °C while the bottom part of tank is 2.6 °C because of buoyancy.

The velocity field in the form of field and streamlines are presented in Fig.9. The average gas velocity inside the tank is under 0.29m/s, which satisfied the expected velocity values for natural convection in the enclosed tank. Heated gas flows through the busbar and VCB in an upward direction can be overserved, which resulted in an effective heat dissipation rate in the top parts of the conductors in comparison of the support insulator part and operating mechanism.

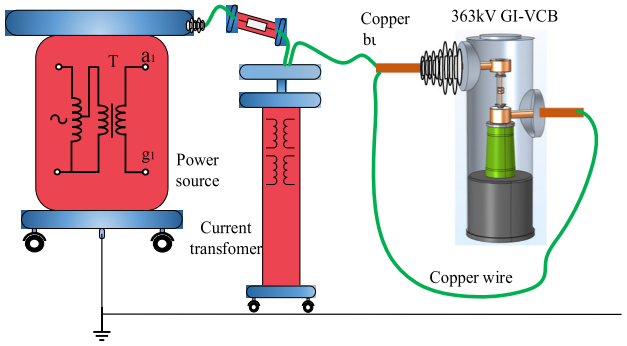

FIGURE 10. Schematic of the temperature rise test.

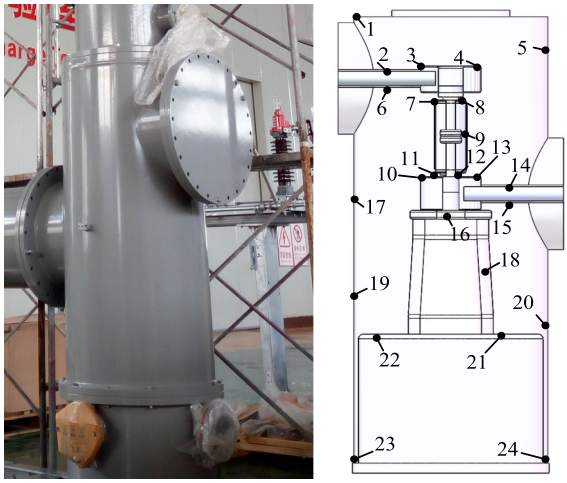

(a) (b)

FIGURE 11. Photo of prototype and locations of sensors. (a) Photography of the prototype. (b) Schematic of thermocouples position.

C. LABORATORY TEST

To verify the simulation results, a single prototype is fabricated and corresponding heat run test is carried out in high voltage laboratory. Fig.10 and Fig. 11 illustrate the set-up of the photo of the 363 kV GI-VCB single prototype and the distributed temperature sensors. In Fig.9, the capacity and voltage level of the power source is 480 kV/80 kA. A current transformer is used to monitor the input current. The 363 kV GI-VCB single tank prototype is connected with the copper wire through 5 m copper busbar [24]–[26]. The ambient temperatrue is controlled by industrial air conditioners. T-type thermocouples and data acquisition unit are installed to measure 24 points in the tank. Sensor 1 is at the top of the tank. Points 2,3,4,6 are on the surface of the bus bar and upconnection terminal. Positions of measuring points 7-8, 11-12

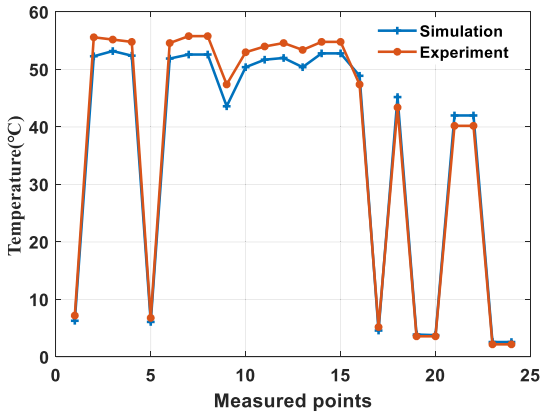

FIGURE 12. Comparison of the simulation and measured temperature for nominal rated current.

TABLE 4. Comparison of simulation and measured temperature.

Part name	Simulation (°C)	Measured (°C)	Difference (°C)
Busbar	52.3	55.6	3.3
Upper terminal	53.2	55.2	2
Bottom terminal	50.4	53.4	3
Transfer flange	48.9	47.4	-1.2
surface of actuator	42.1	40.2	-1.9
Tank (top part)	6.3	7.2	0.9
Tank(bottom)	2.6	2.2	-0.4
Top cap	52.6	55.8	3.2
Bottom cap	52.4	54.6	2.2
Ceramic shell	43.5	47.4	3.9

are at top cap and bottom cap of vacuum chamber. Points 5, 17, 19, 20, 23-24 is placed at the top, middle and bottom of the inner wall of the tank respectively. Sensor 9 is on the ceramic shell of VCB. Measuring points 10, 13-15 are mounted on the bottom connection terminal and lower bus bar. The measuring point 16 and 18 are installed on the surface of connecting flange and epoxy support. Sensor 21-22 are used to monitor the temperature of the actuator.

The test is carried out over a period of time sufficient for the temperature rise to reach a saturated value, which is obtained according to the standards when the increase of the temperature does not exceed 1 °C. All the temperatures are recorded every 30 minutes. Fig. 12 and table 4 shows the comparison of simulation results and experiment results of the 24 points. It can be seen that the calculation results and the temperature test results have the similar variation trend and the maximum discrepancy is 3.9 °C at the point of 12, accounting for 7.9%.

The measured maximum temperature of upper terminal, bottom terminal and busbar are higher than simulated temperature resulted due to the complex structure of contacts as well as the contact resistance, though it's a new prototype, which can produce a little more power loss due to the extremely inhomogeneous distribution current and magnetic field. The measured temperature of transfer flange, actuator and the tank bottom are lower than simulation, because the electromagnetic repulsion mechanism are made of metal which can transfer some heat. Besides, the bolts and some other connection parts were ignored which could enhance the heat conduction and dissipation. Finally, taking into account the overall complexity of the design, still the numerical model accuracy was found to be satisfactory and allows for model application for the future development of the circuit breaker.

V. DISCUSSIONS

A. INFLUENCE OF CONTACT RESISTANCE

The prototype measured in the heating run test is new with very small contact resistance which is 8.2 uΩ. However, according to the reference [27], the contact resistance of VCB had been observed to increase by up to 60% after breaking tests. At that situation, when the vacuum interrupter is closed, the contact of the two contact surfaces is not an ideal surface contact, but a small region due to the surface roughness at the interface, which results in the increase of resistance. The contact resistance would be much bigger after long term operation due to intensive melting and redistribution of melted material of the contacts caused by the large short circuit current. In addition, attenuation of the contact force could give rise to growth of contact resistance. Theoretically, contact resistance can be derived from the resistance of a sphere having radius a representing the physical contact point between two electrical contacts. The equivalent contact resistance is calculated by:

$$R_c = \rho_{el} \cdot \frac{(\pi/2)a}{\pi a^2} = \frac{\rho_{el}}{2a} \tag{24}$$

where the electric resistivity ρ_{el} is that of the bulk contact material at the contact temperature.

The equivalent radius can be calculated from the balance of yield strength σ_y and the material and contact force, F. The yield strength defines the force, where the material begins to deform plastically. In this simulation model, contact resistance is prescribed by creating a circular contact sphere and its radius is described by the following formula:

$$a = \sqrt{\frac{F}{\pi \sigma_y}} \tag{25}$$

For the proposed VCB in this paper, the $\sigma_y = 261N/mm^2$, and the rated contact force $F = 3200N$. However, there are serval contact points. It is a well-known fact that a stable state is obtained for a mechanical support providing three points like a tripod. Multiple contact points can also appear. The resistance is divided into n points, each experiencing $1/n$ of the total contact force. Hence, the equivalent radius is changed to below equation:

$$a = \sqrt{\frac{F}{n\pi \sigma_y}} \tag{26}$$

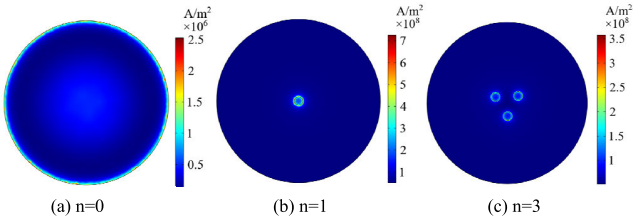

FIGURE 13. Current density of the contact surface at different contact points.

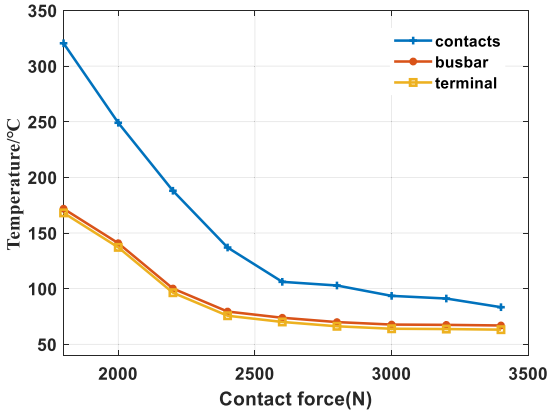

FIGURE 14. Comparison of temperature rise of contacts variation with contact force (n = 1).

Here, we just discuss two situations: $n = 1$ and $n = 3$. In COMSOL simulation, we set the other area as electrical insulation except the contact points where the current flow through. Fig. 13 demonstrates the current density of surface contact at one-point contact and three points contact respectively. When n = 0, the current concentrated on the edge of the contact area; when n = 1, the current can only pass through the small circular contact area with a maximum current density of 7.3E8 A/m^2; when n = 3, the maximum current density drops to 3.7E8 A/m^2 which is still much higher than the good contact. In addition, when the contact force is 1800 N, power losses of the contacts are 923 W and 610.257 W at n = 1 and n = 3 respectively, which is much higher than normal contact.

Fig. 14 and Fig.15 compares the maximum temperature rise of the contacts, busbar and terminal along with increase of the contact force. The contacts' temperature dramatically goes down as well as the busbar and terminals due to the decrease of contact resistance along the increase of contact force. When n = 3, the temperature rise of contacts is much lower than n = 1. Meanwhile, temperature rise of busbar and terminal exceed the IEC limit when contact force is under 2500 N (n = 1) and 2200 N (n = 3). Considering the long-term operation of this 363 kV VCB, the contact resistance and contact force should be carefully monitored.

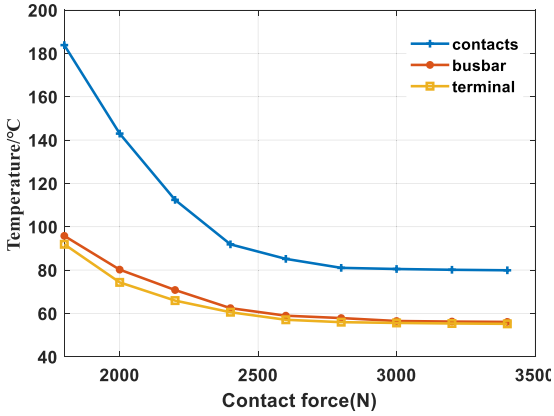

FIGURE 15. Comparison of temperature rise of busbar variation with contact force (n = 3).

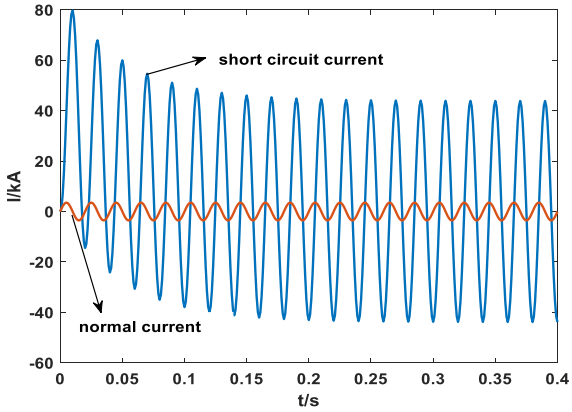

FIGURE 16. Short circuit current waveform of 363 kV power system.

B. INFLUENCE OF THE SHORT CIRCUIT CURRENT

Though the 363 kV GI-VCB can rapidly interrupt the short-circuit current, it has to meet the requirement of rated short-time withstand current 63kA/4s [24]–[26]. Typical short circuit current in 363 kV power system is shown in Fig. 16. Due to the parallel structure, only half of the current flows through the unilateral of 363 kV GI-VCB. The current consists of steady short circuit current and damped impulse current which decays at the time constant of 0.05s in high voltage power system.

Since this current decaying in 0.05s, considering worst situation, we take the effect value of 31.5kA sinusoidal current as the input and calculate the temperature rise during the 4s using the steady temperature as the initial values. Results are shown in Fig. 17. Due to the short circuit current only last for 4s, the heat generated can't dissipate through conduction and convection. And the temperature of contacts and busbar rise almost linearly. The temperature rise of contacts, busbar and terminal are 73.03°C, 60.67°C and 55.48°C respectively. The moving rod, static rod and terminals are solid bulk while the busbar is hollow cylinder which has smaller effective cross section, resulting higher current density. Therefore, the temperature of busbar is higher than contacts and bus bar. This

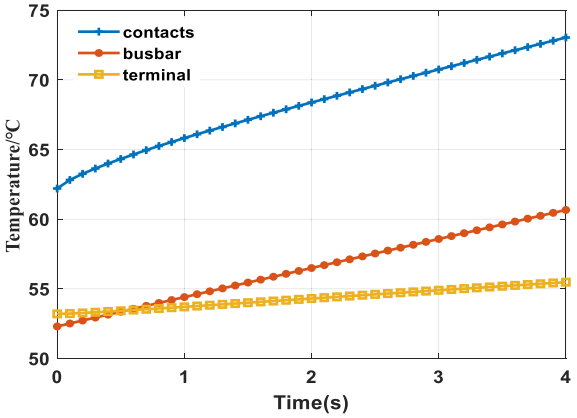

FIGURE 17. Temperature rise variation of contacts, busbar, terminal with time.

also indicates that the proposed 363 kV GI-VCB satisfy the short-stand withstand current requirement.

VI. SUMMARY AND CONCLUSION

In this paper, a novel 363 kV GI-VCB is proposed and 3D coupled electromagnetic-thermal-fluid FEM model is built to assess its thermal performance. The skin effect, temperature-dependent materials properties are taken into account. The vacuum chamber is modelled with temperature dependent effective thermal conductivity and turbulence model is used to describe the heat transfer in gas flow. Temperature rise test was carried out on the prototype to validate the simulation result. Finally, the influence factors are discussed. The following conclusion can be drawn:

(1) The temperature rise of the conductor is ranging from 54°C to 62.2°C, and the contacts in vacuum chamber are the hotspot with temperature of 102.2°C. Under 4s short circuit current, maximum temperature rise of conductors is 73.03 °C. The temperature rises of the proposed GI-VCB at rated condition and short circuit condition both meet the restrictions.

(2) To verify the simulation results, heat run test is conducted at nominal current showing a maximum discrepancy of 3.9 °C at the cap of 40.5kV VCB, accounting for 7.9%. This also proves that the numerical model is accurate to predict the temperature rise of the GI-VCB.

(3) Contact resistance has a great effect on the temperature rise. The validity of the computational model developed can be employed in the design of the whole apparatus to complete the design of this type of circuit breaker. In addition, based on this model, building scenarios with various size levels and ambient temperature conditions can be analyzed.

REFERENCES

[1] X. Yu, Z. Liu, and Y. Chen, "Heat transfer in a high-voltage vacuum circuit breaker," *Proc. Inst. Mech. Eng. A, J. Power Energy*, vol. 225, no. 8, pp. 1099–1110, 2011.

[2] *High-Voltage Switchgear and Control Gear—Part 1 Common Specifications*, International Standard 62271-1, Edition 1.1, 2011.

[3] X. Guan, N. Shu, B. Kang, and M. Zou, "Multiphysics analysis of plug-in connector under steady and short circuit conditions," *IEEE Trans. Compon., Packag., Manuf. Technol.*, vol. 5, no. 3, pp. 320–327, Mar. 2015.

[4] X. W. Wu, N. Q. Shu, H. T. Li, and L. Li, "Contact temperature prediction in three-phase gas-insulated bus bars with the finite-element method," *IEEE Trans. Magn.*, vol. 50, no. 2, Feb. 2014, Art. no. 7006704.

[5] N. Rebzani, E. Clavel, P. Marty, and A. Morin, "Numerical multiphysics modeling of temperature rises in gas insulated busbars," *IEEE Trans. Dielectr. Electr. Insul.*, vol. 23, no. 5, pp. 2579–2586, Oct. 2016.

[6] J. K. Kim, S. C. Hahn, K. Y. Park, H. K. Kim, and Y. H. Oh, "Temperature rise prediction of EHV GIS bus bar by coupled magnetothermal finite element method," *IEEE Trans. Magn.*, vol. 41, no. 5, pp. 1636–1639, May 2005.

[7] M. Bedkowski, J. Smolka, K. Banasiak, Z. Bulinski, A. J. Nowak, T. Tomanek, and A. Wajda, "Coupled numerical modelling of power loss generation in busbar system of low-voltage switchgear," *Int. J. Therm. Sci.*, vol. 82, no. 1, pp. 122–129, Aug. 2014.

[8] M. Bedkowski, J. Smolka, Z. Bulinski, and A. Ryfa, "2.5-D multilayer optimisation of an industrial switchgear busbar system," *Appl. Therm. Eng.*, vol. 101, pp. 147–155, May 2016.

[9] M. Bedkowski, J. Smolka, Z. Bulinski, and A. Ryfa, "Simulation of cooling enhancement in industrial low-voltage switchgear using validated coupled CFD-EMAG model," *Int. J. Therm. Sci.*, vol. 111, pp. 437–449, Jan. 2017.

[10] L. Wang, W. Zheng, L. Wang, J. Lin, X. Li, and S. Jia, "Electromagnetic-thermal-flow field coupling simulation of 12-kV medium-voltage switchgear," *IEEE Trans. Compon., Packag., Manuf. Technol.*, vol. 6, no. 8, pp. 1208–1220, Aug. 2016.

[11] F. Delgado, C. J. Renedo, A. Ortiz, I. Fernández, and A. Santisteban, "3D thermal model and experimental validation of a low voltage three-phase busduct," *Appl. Therm. Eng.*, vol. 110, pp. 1643–1652, Jan. 2017.

[12] M. T. Dhotre, X. Ye, F. Linares, P. Skarby, and S. Kotilainen, "Multiobjective optimization and CFD simulation for a high-voltage circuit breaker," *IEEE Trans. Power Del.*, vol. 27, no. 4, pp. 2105–2112, Oct. 2012.

[13] M. T. Dhotre, J. Korbel, X. Ye, J. Ostrowski, S. Kotilainen, and M. Kriegel, "CFD simulation of temperature rise in high-voltage circuit breakers," *IEEE Trans. Power Del.*, vol. 32, no. 6, pp. 2530–2536, Dec. 2017.

[14] S. Pawar, K. Joshi, L. Andrews, and S. Kale, "Application of computational fluid dynamics to reduce the new product development cycle time of the SF_6 Gas circuit breaker," *IEEE Trans. Power Del.*, vol. 27, no. 1, pp. 156–163, Jan. 2012.

[15] W. H. Lee, J. H. An, Y. J. Kim, and J. C. Lee, "Study on temperature-rise of a 72.5kV vacuum circuit breaker for the higher rated current," in *Proc. 27th Int. Symp. Discharges Elect. Insul. Vac. (ISDEIV)*, vol. 2, Sep. 2016, pp. 1–4.

[16] Q. Wang, H. Wang, Z. Peng, P. Liu, T. Zhang, and W. Hu, "3-D coupled electromagnetic-fluid-thermal analysis of epoxy impregnated paper converter transformer bushings," *IEEE Trans. Dielectr. Electr. Insul.*, vol. 24, no. 1, pp. 630–638, Feb. 2017.

[17] A. G. Fedorov and R. Viskanta, "Turbulent natural convection heat transfer in an asymmetrically heated, vertical parallel-plate channel," *Int. J. Heat Mass Transf.*, vol. 40, no. 16, pp. 3849–3860, 1997.

[18] L. Shao and S. B. Riffat, "Accuracy of CFD for predicting pressure losses in HVAC duct fittings," *Appl. Energy*, vol. 51, no. 3, pp. 233–248, 1995.

[19] A. Behzadmehr, N. Galanis, and A. Laneville, "Low Reynolds number mixed convection in vertical tubes with uniform wall heat flux," *Int. J. Heat Mass Transf.*, vol. 46, no. 25, pp. 4823–4833, 2003.

[20] J. K. Sigey, F. K. Gatheri, and M. Kinyanjui, "Numerical study of free convection turbulent heat transfer in an enclosure," *Energy Convers. Manage.*, vol. 45, nos. 15–16, pp. 2571–2582, 2004.

[21] R. Nowak, B. Samul, and V. L. Oganezov, "A 3-D Electrothermal Simulation of the Outdoor Medium-Voltage Circuit Breaker," *IEEE Trans. Power Del.*, vol. 34, no. 12, pp. 572–579, Apr. 2019.

[22] *Heat Transfer Module User's Guide*. COMSOL Multiphysics v. 5.4., COMSOL AB, Stockholm, Sweden, 2018.

[23] *CFD Module User's Guide*, COMSOL Multiphysics v. 5.4., COMSOL AB, Stockholm, Sweden, 2018.

[24] *High-voltage Switchgear and Control Gear—Part 100 Alternating-Current Circuit-Breakers*, IEC Standard 62271-100, 2017.

[25] *Common Specifications for High-Voltage Switchgear and Control Gear*, China's National Standard GB/T Standard 11022-2011, 2011.

[26] *High-Voltage Alternating Switchgear and Control Gear*, China's National Standard GB/T 1984-2014, 2014.

[27] E. Dullni, D. Gentsch, W. Shang, and T. Delachaux, "Resistance increase of vacuum interrupters due to high-current interruptions," *IEEE Trans. Dielectr. Electr. Insul.*, vol. 23, no. 1, pp. 1–7, Feb. 2016.

XIAO YU received the bachelor's degree from the School of Electrical Engineering, Chongqing University, China, in 2015, where he is currently pursuing the Ph.D. degree. He is also a Visiting Academic with the University of Warwick, U.K. His research interest includes the reliability of power equipment, the multi-physics modeling and calculation for circuit breakers, and condition evaluation of power equipment.

FAN YANG received the Ph.D. degree from Chongqing University, Chongqing, China, in 2008, where he is currently a Professor and the Vice Dean of the Department of Electrical Engineering. He has been conducting research in the areas of electromagnetic-thermal coupled field calculation and fault diagnosis of high-voltage equipment. He has published more than 50 articles in reputed journals and conferences. He is a member of the International Electromagnetic Field Computing Society.

GAO BING received the Ph.D. degree from the School of Electrical Engineering, Chongqing University, Chongqing, China, in 2016, where he is currently a Lecturer. His research interests include the reliability of power modules, the multi-physics coupling field calculation for power electronics, and the development of condition monitoring methods for power electronic converters.

HENG LIU, photograph and biography not available at the time of publication.

XING LI, photograph and biography not available at the time of publication.

SHAOGUI AI, photograph and biography not available at the time of publication.

XUXIANG WU, photograph and biography not available at the time of publication.